EFFECTS of HYPERTENSION and PRESSURE GRADIENT in A HUMAN CEREBRAL ANEURYSM USING FLUID STRUCTURE INTERACTION SIMULATIONS

Article *in* Journal of Mechanics in Medicine and Biology · February 2017

DOI: 10.1142/S021951941750018X

CITATIONS
4

READS
232

2 authors:

Alvaro A Valencia
University of Chile
79 PUBLICATIONS **1,340** CITATIONS
SEE PROFILE

Francisco Torres
1 PUBLICATION **4** CITATIONS
SEE PROFILE

Journal of Mechanics in Medicine and Biology
Vol. 17, No. 1 (2017) 1750018 (17 pages)

DOI: 10.1142/S021951941750018X

World Scientific
www.worldscientific.com

EFFECTS OF HYPERTENSION AND PRESSURE GRADIENT IN A HUMAN CEREBRAL ANEURYSM USING FLUID STRUCTURE INTERACTION SIMULATIONS

ALVARO VALENCIA* and FRANCISCO TORRES

Department of Mechanical Engineering
Universidad de Chile, Beauchef 851
Santiago 8370456, Chile
**alvalenc@ing.uchile.cl*

Received 8 June 2015
Revised 11 November 2015
Accepted 11 November 2015
Published 30 March 2016

Fluid–structure interaction (FSI) simulations were carried out in a human cerebral aneurysm model with the objective of quantifying the effects of hypertension and pressure gradient on the behavior of fluid and solid mechanics. Six FSI simulations were conducted using a hyperelastic Mooney–Rivlin model. Important differences in wall shear stress (WSS), wall displacements, and effective von Mises stress are reported. The hypertension increases wall stress and displacements in the aneurysm region; however, the effects of hypertension on the hemodynamics in the aneurysm region were small. The pressure gradient affects the WSS in the aneurysm and also the displacement and wall stress on the aneurysm. Maximum wall stress with hypertension in the range of rupture strength was found.

Keywords: FSI; CFD; cerebral aneurysm; rupture risk factor; hypertension.

1. Introduction

A cerebral aneurysm is an abnormal dilatation of the arteries and is located in the subarachnoid space at the base of the brain. Hypertension and smoking play a major role in its formation, growth, and rupture. A reduction of the tunica media, and middle muscular layer on the artery wall combined with hemodynamic factors lead to this process.[1] A study of unruptured cerebral aneurysms has found that the rupture rate for larger aneurysms (> 10 mm diameter) is 0.5% and that the rupture of the aneurysm produces subarachnoid hemorrhage with severe neurological damages for the patient.[2]

Computational fluid dynamics (CFD) studies using cerebral aneurysm models have suggested a relationship between the hemodynamics through the wall shear

*Corresponding author.

stress (WSS) and the aspect ratio on the risk of rupture.[3] Low WSS triggers an inflammatory pathway, while high WSS triggers a mural-cell-mediated pathway, and these changes in the WSS could be associated with the growth and rupture of cerebral aneurysms.[4] The probability of aneurysm rupture as a function of geometry, low WSS, and the oscillatory shear index in the data of 204 samples was recently reported.[5] In vertebrobasilar aneurysms, the space averaged velocity at peak systole increased by 30% in hypertension whereas the flow decreased by 20% in hypotension in CFD simulations reported in Ref. 6

The rupture stress and the corresponding stretch obtained by uniaxial tests of human cortical arteries are 4.07 MPa and 1.42, respectively, in specimens obtained by surgery.[7] The rupture stress in samples of a human cerebral aneurysm in an axial test was between 0.7 and 1.6 MPa for vulnerable and strong aneurysms, respectively.[8] Other works report that the average rupture strength in a cerebral aneurysm ranges from 0.73 to 1.9 MPa, depending on the measured directions, due to aneurysm wall anisotropy.[9] The cerebral aneurysm wall is weaker than a normal artery wall, and therefore it is more sensitive to the mechanical load produced by the hemodynamics through the blood pressure.

Solid mechanics simulation, performed by Ref. 10 of sphere-shaped cerebral aneurysms with a wall thickness of 0.033 mm, assuming a maximum wall strength of 1.5 MPa, showed that aneurysms with a radius of 4.5 mm were at risk of rupture with hypertension. In a mechanical study of 30 patient-specific models of cerebral aneurysms,[11] the effects of hypertension was reported in one case. The maximum displacement increases by 23% (0.32 mm) and the maximum wall stress increases by 58% (1.77 MPa) with respect to the corresponding values with normal pressure.

Fluid–structure interactions (FSI) simulation using image-based models of human cerebral aneurysms can help to better understand the vascular remodeling processes associated with aneurysm growth and rupture.[12] FSI simulation with normal and high blood pressures shows that WSS and the mechanical stress in the aneurysmal wall are strongly affected by hypertension.[13] The use of linear elastic material or the Mooney–Rivlin hyperelastic model to characterize the aneurysmal wall has important effects on the prediction of deformation and WSS on the aneurysm wall.[14] In a comparison between WSS obtained using rigid (CFD) and flexible walls (FSI), it was shown that the rigid wall simulation overestimated the WSS by as much as 52% in one of the investigated models.[15]

Using FSI simulations in 10 patient-specific models, half of which ruptured, the WSS, arterial wall stress, and stretch were compared. The maximum stress and stretch were around 1.4 MPa and 1.5, respectively.[16] The patient-specific risk of rupture could be based on aneurysm volume variation calculated using FSI simulations, considering soft (close to rupture) and stiff (healthy) aneurysms.[17] The classification of soft, rigid, and intermediate aneurysm walls was investigated in Ref. 18 through uniaxial mechanical tests on human aneurysm specimens, and it was found that all unruptured aneurysms presented a more rigid tissue than ruptured or pre-ruptured aneurysms within each gender subgroup.

FSI and computational structural simulations of human cerebral aneurysms using their own wall mechanical properties were recently presented in Ref. 19. An averaged pulse obtained from 36 patients with cerebral aneurysms was used for the inlet velocity and an oscillating pressure difference was used for the outlet pressure. A high stress of around 0.8 MPa was reported using FSI and Mooney–Rivlin models. The FSI model needs accurate image-based geometry but also the wall thickness and mechanical wall properties of a specific aneurysm. Obtaining these values *in vivo*to predict the rupture risk using FSI is an important challenge.

The inlet velocity conditions also affect the simulations of cerebral aneurysms, and significant differences in WSS and oscillating shear stress index (OSI) were found between Womersley and plug-flow boundary conditions.[20] Considering the same mean inlet flow rate, different waveforms produced similar WSS distributions but different OSI magnitudes on the aneurysm.[21]

The objective of the present investigation is to report the effect of hypertension and pressure gradient by implementing FSI simulations using the cerebral aneurysm model described in Ref. 19. The methodology is similar, but in this work we have implemented a Windkessel model to estimate the physiological boundary conditions better.

2. Methodology

The sample tissue was delivered by an aneurysm surgery, and a 3D angiography image was reconstructed to obtain an adequate geometry for the simulation software ADINA (see Fig. 1). The aneurysm thickness of 350μm was measured with an

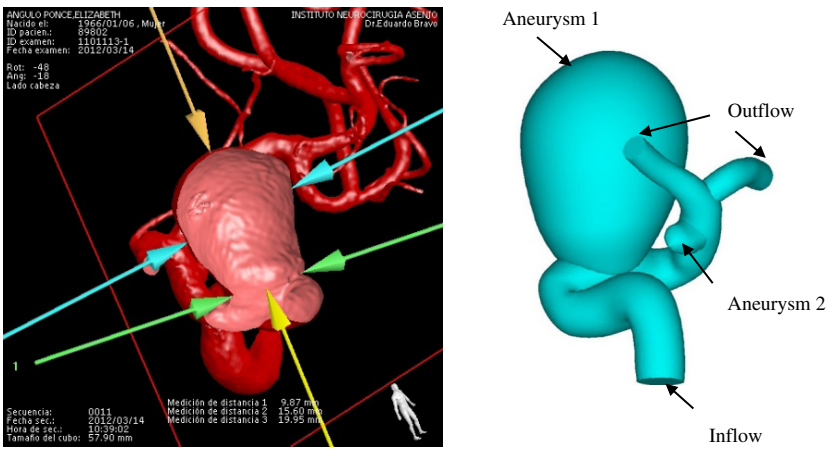

(a) (b)

Fig. 1. (a) 3D rotational angiography of the aneurysm of the left carotid ophthalmic aneurysm and (b) CAD obtained from the reconstruction of the original angiography showing principal parts of the domain.

optical digital microscope, and for the artery a normal thickness of 400μm was assumed.[22]

The fluid flow was modeled using the conservation of mass and momentum or Navier–Stokes equations. The blood is considered non-Newtonian fluid, the Carreau model was used to model the shear thinning behavior of blood, and the values for the model were taken from Ref. 23.

The FSI simulations show that the displacements of the fluid and the solid are compatible and the tractions are in equilibrium. The mechanical properties of the wall are a relevant input for the FSI simulations.

The aneurysm was extracted using surgical clipping, the sample was mechanically tested using a tensile device,[22] and the experimental data were fitted using a Mooney–Rivlin hyperelastic model with five constants, expressed by Eq. (1).

$$W = c_{10}(I_1 - 3) + c_{01}(I_2 - 3) + c_{11}(I_1 - 3)(I_2 - 3) + c_{20}(I_1 - 3)^2 + c_{02}(I_2 - 3)^2. \tag{1}$$

$c_{10} = 0.429$, $c_{01} = -0.119$, $c_{11} = 0.585$, $c_{20} = 0.579$, and $c_{02} = 0.564$ MPa are the material hyperelastic constants. These mechanical properties of the aneurysm are used in the following FSI simulation. The hyperelastic Mooney–Rivlin model postulated a relation between the strain energy function W for rubber with the first and second strain invariants, I_1 and I_2, of the right Cauchy-Green deformation tensor. The Mooney–Rivlin model provides a better description of the behavior of aneurysmal tissue.[22]

2.1. *Boundary conditions*

For the investigation of the effects of hypertension we have developed a code that includes velocity and pressure variations. The inlet velocity and the inlet and outlet pressure were calculated in this investigation using a Windkessel model and the Womersley solution for a pulsatile flow in a tube.

To obtain the physiological flow conditions at the artery inlet, we used the Womersley velocity profile, which is the solution of unsteady flow in a tube with an oscillating pressure gradient. The solution depends on the Womersley number, $\alpha = R^*(\omega/\nu)^{0.5}$, where R is the artery radius, ω is the angular frequency, and ν is the kinematic viscosity of the fluid. It is a measure of the ratio of the unsteady part of the momentum equation to the viscous part. When α is small, the unsteadiness is not important, and the solutions become Poiseuille solutions that vary in magnitude but not in shape. If α is large, the shapes of the profiles are not parabolic.[24] In this case $\alpha = 3.7$ and therefore the inlet profile is parabolic with time variation.

The Womersley solution for the velocity profile in a straight tube using a Matlab code for the profile calculation and later export to ADINA software was implemented. The Womersley solution equation is described in more detail in Ref. 24 Numerical tests performed have shown that after the second cardiac cycle, the fluid and solid results do not change, and therefore the present results are for the third

cardiac cycle. The implementation of the Windkessel method is described in the following section.

2.1.1. *Three-element Windkessel model for outflow boundary conditions*

Lower dimensional models have been used in previous studies with the goal of deriving outflow boundary conditions that yield physiologically realistic flow patterns and pressure distributions in the fluid computational domain. Lumped parameter models using electric circuit analogies for calculating flow rates and pressure are widely implemented.[25] In these models, it becomes necessary to quantify secondary variables that represent the momentum transfer of the fluid at the defined nodes. The accuracy of the solution will depend on how these variables are quantified and on the type of electric circuit model. Windkessel models have been implemented in a variety of applications in the cardiovascular system.[25] There are at least three relevant Windkessel configurations that account for the modeling of viscous, inertial, and compliance effects.[25]

In this work, we used a three-element Windkessel model with two resistors and a capacitance. The capacitance allows us to use a constitutive equation to model the arterial wall material properties. With this approach, we obtain the pressure and flow rate at the desired outflow boundaries. The derivation of the proposed model is made under the assumption of pressure continuity from the parent to the daughter branches of the vascular network.

In the following, we illustrate the application of the variable capacitance Windkessel model to obtain the outflow pressure waveforms for the vascular network. The corresponding electrical circuit analog of this geometry is shown in Fig. 2.

The flow rate $q_3(t)$ through the capacitance C_1 shown in Fig. 2 is given by

$$q_3(t) = C_1 \frac{dp_1}{dt}, \tag{2}$$

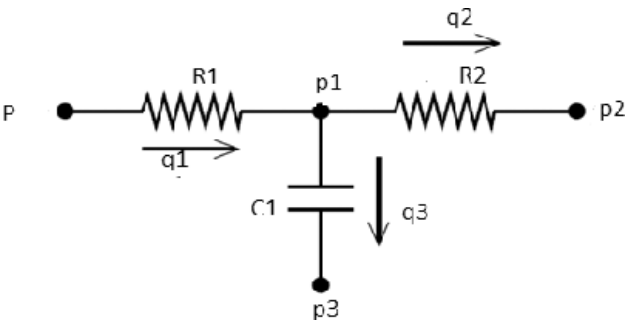

Fig. 2. Schematic of the electrical circuit analogy for the three-element Windkessel model: the unknown variables are the flow rates q_2 and q_3 and the outflow pressures p_2 and p_3. The model simulates the blood flow through a vessel like an electrical circuit with a resistance and an impedance to consider the compliance of the vessel.

where p is the pressure, t is the time, and the pressure drop through resistances R_1 and R_2 is

$$p(t) - p_1(t) = R_1 q_1(t), \tag{3}$$

$$p_1(t) - p_2(t) = R_2 q_2(t). \tag{4}$$

By Kirchhoff's law of conservation of flow rate at the junction p_1,

$$q_3(t) + q_2(t) = q_1(t), \tag{5}$$

where $q_2(t)$ and $q_3(t)$ are the flow rates exiting the domain. By substituting Eqs. (2)–(4) into Eq. (5), we obtain

$$C_1 \frac{dp_1(t)}{dt} + \frac{p_1(t) - p_2(t)}{R_2} = \frac{p(t) - p_1(t)}{R_1}. \tag{6}$$

Thus, the pressure at the exit is given by

$$p_2(t) = R_2 C_1 \frac{dp(t)}{dt} - R_1 R_2 C_1 \frac{dq_1(t)}{dt} + p(t) - (R_1 + R_2) q_1(t) \tag{7}$$

which gives an expression for $p_2(t)$ that is a function of $p(t)$, $q_1(t)$, and the resistance and compliance variables. The capacitance C_1 and the resistance components R_1 and R_2 are obtained by

$$C_1 = \frac{3ALr}{2Eh}, \tag{8}$$

$$R_1 = \frac{8 c_v L \mu}{\pi r^4}, \tag{9}$$

$$R_2 = \frac{P_0}{Q}, \tag{10}$$

where L is the aneurysm length, A is the area, h is the aneurysm wall thickness, μ is the dynamic viscosity, and r is the radius of the vessel segment. The elastic modulus of the aneurysm is E and c_v is a constant that depends on the Womersley number α defined in the previous section. Q is the blood flow ($Q = vA$ m^3/s); P_0 is the minimum pressure of the circulatory system and is approximately $P_0 = 100$ Pa for large veins Ref. 26. The elastic modulus for the aneurysm was calculated by Eq. (11) using the material constant of the Mooney–Rivlin model, giving $E = 1.86$ MPa.[27]

$$E = 6(c_{10} + c_{01}). \tag{11}$$

For the hypertension, we used the pressure ranges defined in Ref. 28 and we calculated the FSI simulations for one normal and three hypertensive states; the pressure profiles for the one normal and three hypertensive cases are shown in Fig. 3(a). The constant $c_v = 1.1$ was obtained from Ref. 26. The parameters obtained for this model are $C_1 = 7.77 \times 10^{-11}$ m^5/N, $R_1 = 4.78 \times 10^4$ Ns/m^5, $R_2 = 1.92 \times 10^7$ Ns/m^5 (large outlet), $R_2 = 2.23 \times 10^7$ Ns/m^5 (small outlet), and $Q = 9.66 \times 10^{-6}$ m^3/s for the base case.

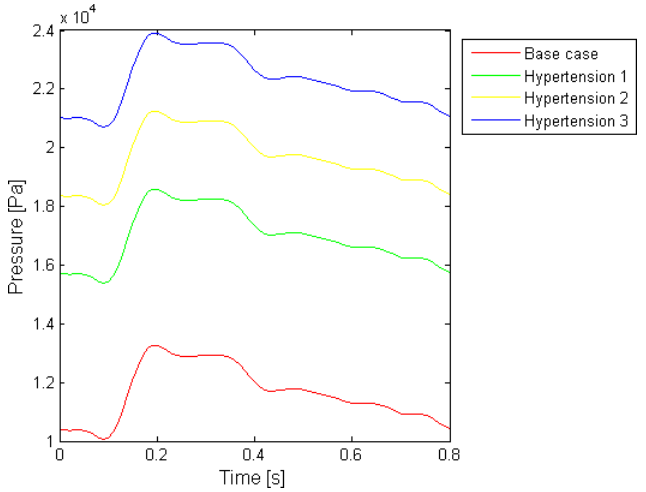

(a)

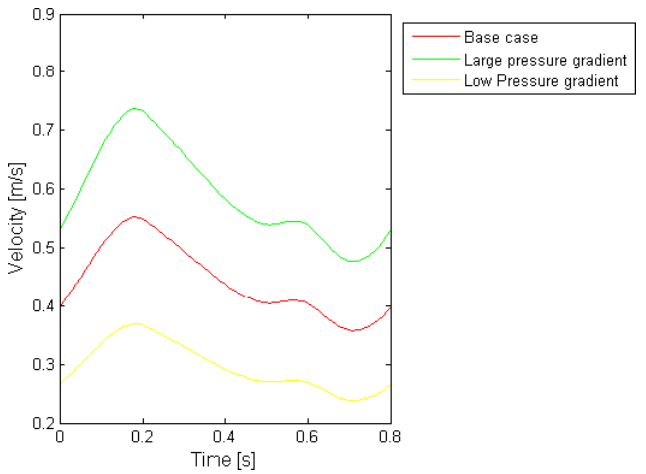

(b)

Fig. 3. (a) Pressure pulse for the base and hypertensive cases. (b) Inlet velocity pulse for the base case and low and high pressure gradients.

The axial pressure gradient for the base case has a minimum at around –3800 Pa/m and a peak velocity of 0.54 m/s; for the small pressure gradient we used –2500 Pa/m with a peak velocity of 0.35 m/s and for the large pressure gradient we used –5000 Pa/m with a peak velocity of 0.75 m/s (see Fig. 3(b)).

2.2. *General considerations and numerical method*

In this investigation, six FSI simulations were carried out including the base case, three hypertensive cases, and two pressure gradients. The FSI simulations were

performed with hyperelastic Mooney–Rivlin material using 3D shell elements. The FSI simulations were completely coupled with the CFD simulation in which an equilibrium of strength and displacements between solid and fluid is sought for every time step.

The FSI simulations were solved by the software ADINA 8.8.0. The maximum number of iterations in a time step was 100, the energy tolerance was 0.001, and the time step was 0.01 s. We used the formulation with large displacements and small stains in the FSI calculation available in ADINA.[27] The unstructured grid was composed of tetrahedral elements with four-node elements in the fluid and four-node isoparametric elements for the solid shell.

Five grid sizes in the fluid of 0.30, 0.33, 0.40, 0.50, and 0.70 mm were used to determine the optimal grid size, the difference in WSS at a control point between the grid sizes of 0.30 and 0.40 mm was 12%, and the difference in maximum pressure was 1%. We used the grid size of 0.40 mm in the present FSI simulations. Figure 4 shows the grid, the inlet velocity profile, and the outlet pressure boundary conditions during diastole.

The rupture point in a cerebral aneurysm is located in the aneurysm fundus, and for this reason we define the control point in the fundus and report the maximum wall stress and also the wall stress at this control point.

3. Results and Discussion

Figure 1 shows the 3D rotational angiography of the aneurysm of the left carotid ophthalmic aneurysm obtained with a Philips Integris Allura 3D rotational angiograph and the reconstructed CAD model, which has two aneurysms, but the

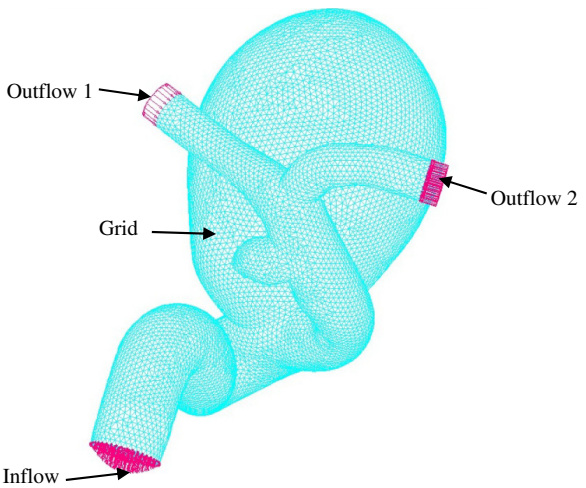

Fig. 4. Grid and boundary conditions at diastolic time. The inlet velocity distribution with the radius at the inlet and the pressure boundary condition at outflows 1 and 2 are shown.

following results and discussions are based on the large aneurysm, which is the principal pathology in this patient. The results of the small aneurysm are not analyzed in detail because it is an incipient pathology and cannot be classified as a saccular aneurysm.

The velocity magnitude distribution for two perpendicular planes for the base case at systolic ($t = 1.9\,\text{s}$) and diastolic time ($t = 2.4\,\text{s}$) is shown in Fig. 5. The differences in velocity magnitude during systole and diastole are important, but the locations of the maximum and minimum do not change. The blood enters the aneurysm, flows parallel to the wall, and produces a vortical structure inside the aneurysm. Because of the time-dependent nature of the inflow boundary condition,

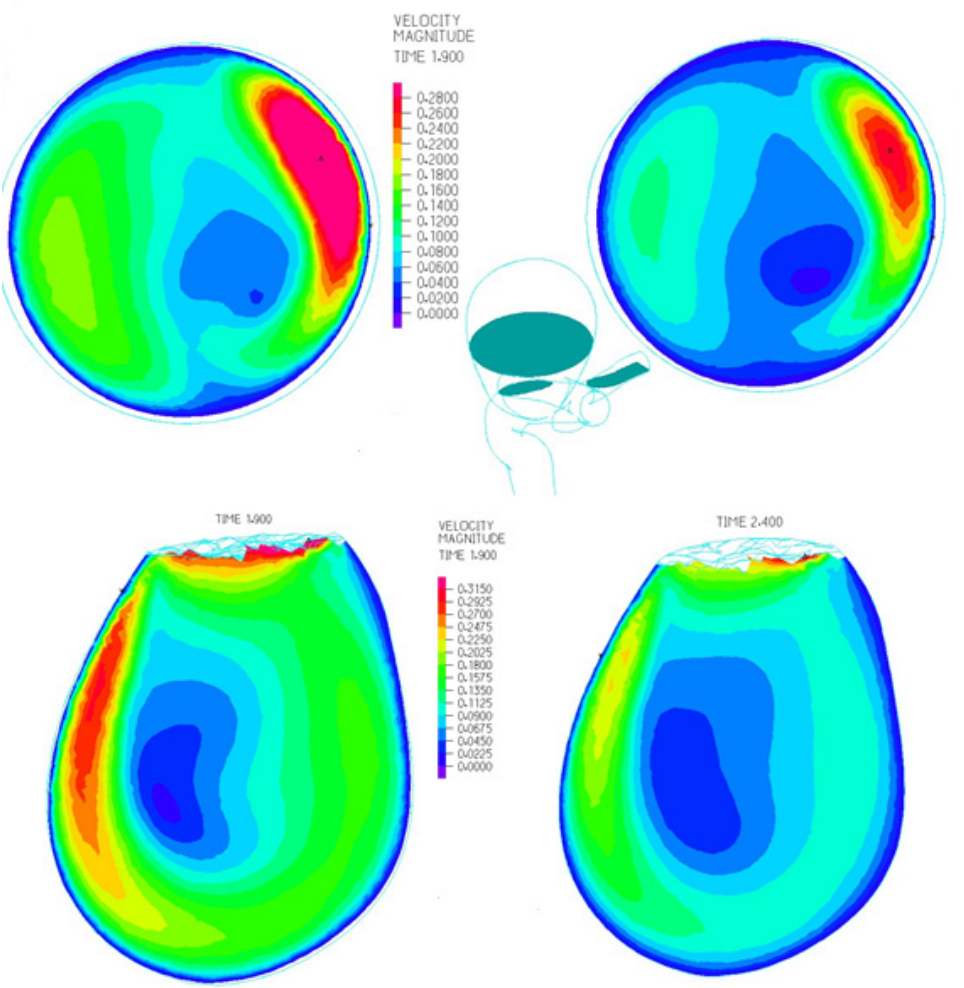

Fig. 5. Velocity magnitude at systolic time ($t = 1.9\,\text{s}$) and at diastolic time ($t = 2.4\,\text{s}$) for the base case in two perpendicular planes.

the flow in the aneurysm is characterized by vortices that are continuously increasing and decreasing in size within the sac.

A comparison of the WSS distributions during systole between the base case and the large pressure gradient is shown in Fig. 6. The WSS on the aneurysm is lower compared with the WSS on the cerebral arteries, due to the small velocity magnitude inside the aneurysm. The pressure gradient affects the WSS in the model, and increases in the pressure gradient increase the velocity magnitude and therefore the WSS; the maximum WSS on the arteries increases by 35%. The effect of hypertension on the WSS is very small because the inlet velocity distribution is the same in all hypertensive cases.

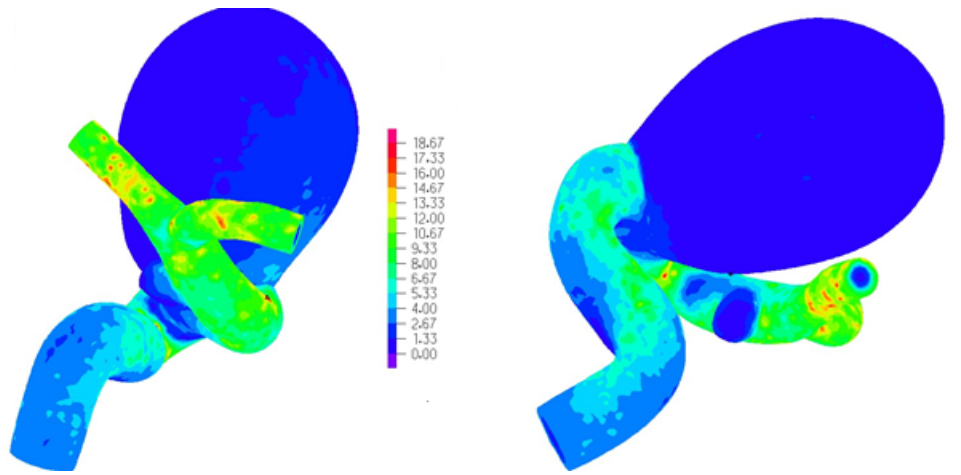

(a)

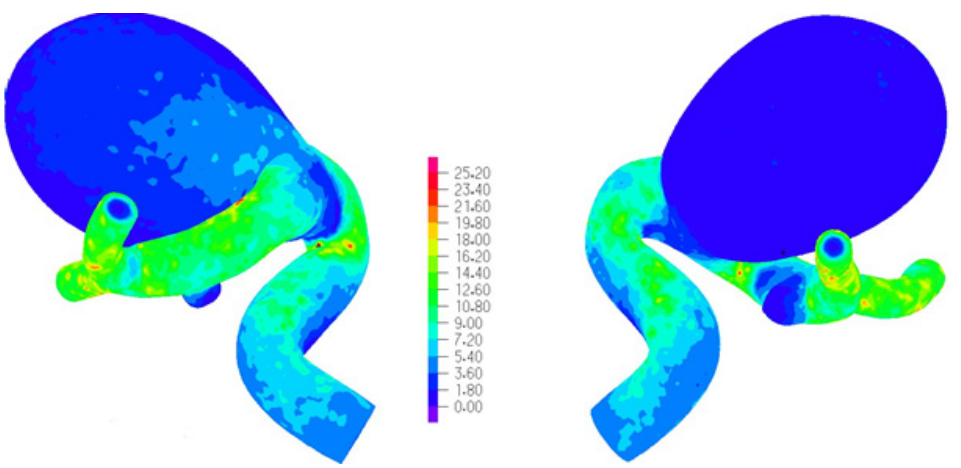

(b)

Fig. 6. WSS distribution at systolic time: (a) base case and (b) large pressure gradient.

A comparison of the displacement magnitude between the base case and the hypertensive case 3 during systole are shown in Figs. 7(a) and 8(a). The large displacement is located in the aneurysm dome. The increases in displacement magnitude due to hypertension are relevant and the maximum displacement increases by 32%. The zones with larger displacement in the aneurysm are

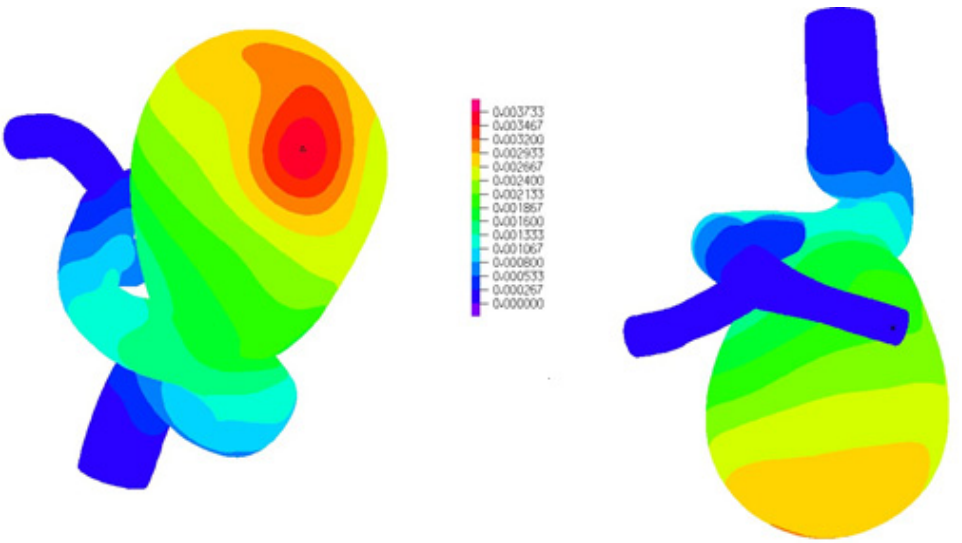

(a)

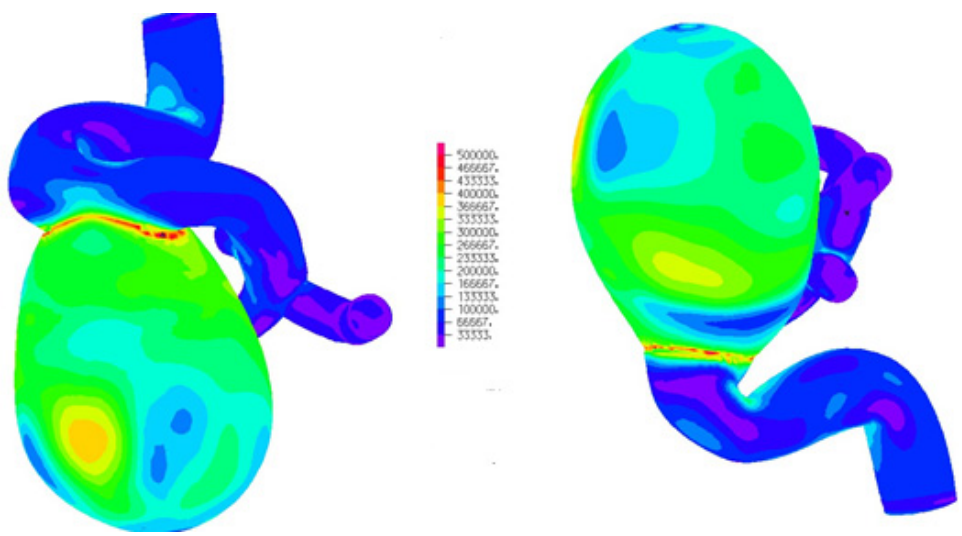

(b)

Fig. 7. (a) Displacement distribution for the base case at systolic time. (b) Effective stress distribution at systolic time for the base case.

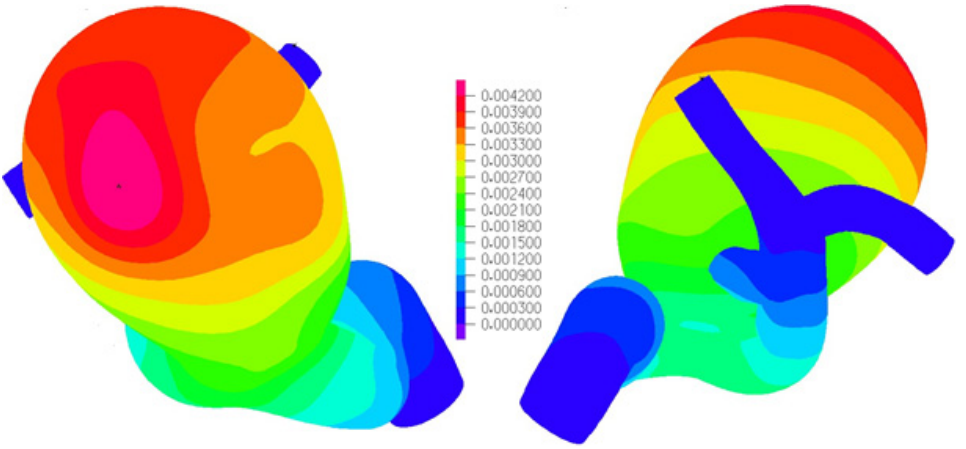

(a)

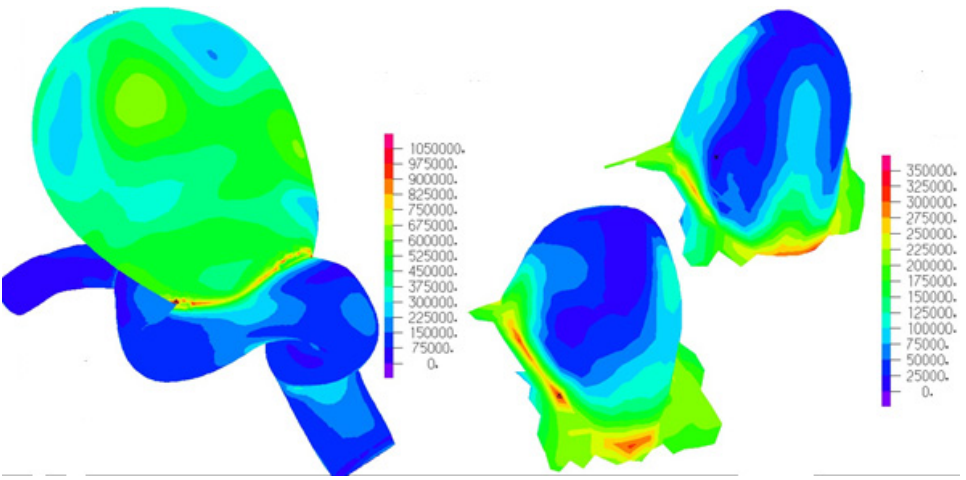

(b)

Fig. 8. (a) Displacement distribution for the hypertensive case 3 at systolic time. (b) effective stress distribution at systolic time for the hypertensive case 3. The figure also shows the stress distribution on the small aneurysm.

important. The displacements in the aneurysm are larger compared with the displacements in the normal artery; the artery wall is thicker than the aneurysmal wall.

The effective stress on the aneurysm is strongly affected by the hypertension. Figure 7(b) shows the effective stress distribution for the base case: the maximum stress is located at the aneurysm neck and reaches 582 kPa. The stress is larger in the aneurysm compared with the proximal arteries. The distribution on the aneurysm dome is regular. The effective stress distribution for the hypertensive case 3 is

shown in Fig. 8(b): the maximum effective stress on the aneurysm neck is 1110 kPa. The increase in effective stress is 91%. The stress in the aneurysm dome increases by a factor of almost two. Figure 8(b) also shows the effective stress distribution on the small aneurysm; the values of stress are similar to the values for the proximal artery.

The temporal evolution of the effective stress on the aneurysm fundus (control point) and maximum value located on the aneurysm neck for the base case and the three hypertensive cases is shown in Fig. 9. The effect of hypertension is relevant: the maximum stress can reach 1.1 MPa at systole for hypertension state 3. The effective stress on the aneurysm fundus is lower compared with the values in the aneurysm neck and dome (see Fig. 8(b)). The time dependence of the effective stress is similar and changes the values between the different cases and locations. The increase in effective stress with increases in hypertension pressure is not linear.

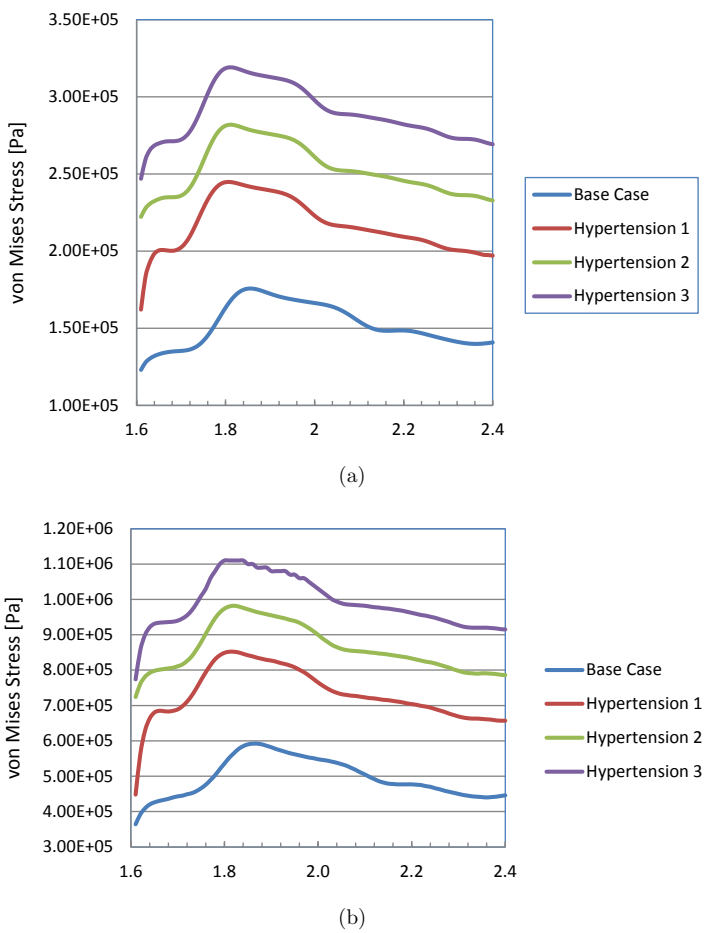

Fig. 9. Von Mises temporal evolution for the base case and for the three hypertensive cases: (a) control point at aneurysm fundus and (b) maximum stress point.

Table 1. Maximum WSS, effective stress, first principal stress, displacement in the aneurysm, and effective stress at aneurysm fundus at systole.

Case	WSS [Pa]	Effective stress [kPa]	First principal stress [kPa]	Displacement [mm]	Effective stress fundus [kPa]
Base case	20.8	592	617	3.67	175
Hypertension 1	19.32	852	884	4.31	245
Hypertension 2	19.04	982	1020	4.57	282
Hypertension 3	18.83	1110	1150	4.84	316
High pressure	26.8	705	733	4.12	210
Low pressure	14.2	514	544	3.35	155

Table 1 shows the maximum WSS, effective stress, first principal stress, and displacement in the aneurysm during systole as well as the effective stress at the aneurysm fundus (control point) during systole. The increase in effective stress in the neck (maximum stress) with hypertension is very relevant and can reach more than 1.1 MPa. The stress on the fundus can be 81% higher than with the normal pressure. A change in the pressure gradient changes the wall stress and displacement, as reported in Table 1, due to a change in blood flow with respect to the normal pressure gradient. The effects of hypertension on WSS in the aneurysm were small. On the contrary the effects of pressure gradient or inlet velocity magnitude on WSS were important.

The maximum wall stress for the hypertensive case 3 was 1.1 MPa (see Table 1). This value is close to the rupture strength of the affected tissue, and the maximum is located on the aneurysm neck. However, the wall stress on the aneurysm fundus is lower, but if a remodeling process that reduces the wall thickness occurs in the pathological tissue near the fundus, the aneurysm can rupture. Ultimate stresses ranging from 0.7 MPa to 1.6 MPa were found in uniaxial tests on vulnerable and strong unruptured cerebral aneurysms. The mechanical characteristics of the aneurysm could be divided into two classes: low failure stress and pressure (vulnerable) and high failure stress and failure pressure (strong).[8] The present FSI results with hypertension are in this range of wall stress. The stretch ratio and rupture strength of six samples of the affected tissue ranged from 1.28 to 1.50 and from 1.09 MPa to 2.47 MPa, respectively.[22]

In a CFD study of eight unruptured intracranial aneurysms, the ultimate strain was correlated negatively with the aneurysm inflow rate, mean velocity, and mean WSS.[29] This investigation links hemodynamics with aneurysm wall properties; these relationships need to be tested with larger aneurysm samples.

Lee *et al.*[30] have shown that ruptured aneurysms exhibit larger wall displacement at the dome, lower WSS, and higher effective stress than unruptured aneurysms, regardless of elasticity or blood pressure. The results suggest that the aneurysm rupture is affected by aneurysm morphology and that hypotension contributes to rupture by amplifying the effect of expansion.

An aneurysm wall modeled with an isotropic material resulted in an underestimation of both maximum principal stress and stretch compared to the isotropic material model in patient-specific models simulated using FSI.[31] For the three aneurysm geometries, anisotropic peak wall stresses were approximately 50% higher than for an isotropic material. The material parameters for anisotropic and isotropic materials were obtained from data for healthy arteries.

The rupture strength of tissues can change with the age of the patient and can be associated with changes in the structure of the extracellular matrix due to changes in collagen fibrils with increasing age. The influence of the collagen-fibril volume fraction on the tensile properties of tendons has been reported in Refs. 32 and 33, and this effect should be investigated in cerebral aneurysms. The reinforcement mechanism of tissues is related with the underlying mechanism of elastic fiber reinforcement; the key findings on the mechanical response of extracellular matrix at the respective levels of the hierarchical architecture are described in Ref. 34. The mechanical response represented by a stress–strain curve can be divided into five regions corresponding to the respective mechanical processes, namely toe-to-heel, elastic deformation, yielding, plastic deformation, and rupture. The processes occurring at the collagen fiber level involve decrimping, elastic deformation by fiber–fiber sliding, fiber yielding, plastic deformation, and fiber defibrillation or rupture.[34] Apoptosis in the aneurismal tissue can also affect the mechanical integrity of the wall; apoptosis is preponderant in capillary endothelial cells.[35]

Finally we may note that this investigation has various limitations. The aneurysm wall thickness can vary and therefore the wall stress distribution and deformation could change. The model does not include direct interactions with the surrounding vasculature and cerebral tissue. The experimental mechanical properties were obtained using uniaxial tests; however, the aneurysm tissue *in vivo* is closer to equibiaxial loading. FSI models including biological degenerative mechanics are necessary to consider local aneurysm wall reduction in order to explain cerebral aneurysm rupture at the fundus.

4. Conclusions

In this work, the effect of hypertension and pressure gradient on a human cerebral aneurysm model using the aneurysm own mechanical properties was investigated using FSI simulations. The hypertension state increased the wall stress and deformation, and the effects of hypertension on hemodynamics in the aneurysm were small. In contrast, the effects of pressure gradient or inlet velocity magnitude on aneurysm hemodynamics were important.

The aneurysm rupture is mostly located at the fundus and in this region the wall stress is low compared with the rupture stress, but if a remodeling process that reduces the wall thickness occurs in the pathological tissue, the aneurysm can be vulnerable. More complex models that include biological degenerative mechanics are necessary to determine the rupture risk in cerebral aneurysms.

Acknowledgments

The financial support received from FONDECYT under project 111008 and the Center for Mathematical Modeling under grant no. PFB03 2007 of Universidad de Chile is gratefully acknowledged.

Conflict of Interest

The authors have no conflict of interest in relation to any organization with respect to the publication of this paper.

References

1. Brisman J, Song J, Newell D, Cerebral aneurysms, *New Engl J Med* **355**:928–939, 2006.
2. Wardlaw JM, White PM, The detection and management of unruptured intracranial aneurysms, *Brain* **123**:205–221, 2000.
3. Zeng Z, Durka M, Kallmes D, Ding Y, Robertson A, Can aspect ratio be used to categorize intra-aneurysmal hemodynamics? A study of elastase induced aneurysms in rabbit, *J Biomech* **44**:2809–2816, 2011.
4. Meng H, Tutino VM, Xiang J, Siddiqui A, High WSS or low WSS? Complex interactions of hemodynamics with intracranial aneurysm initiation, growth, and rupture: Toward a unifying hypothesis, *Am J Neuroradiol* **35**(7):1254–1262, 2013.
5. Xiang J, Yu J, Snyder K *et al.*, Hemodynamic-morphological discriminate models for intracranial aneurysm rupture remain stable with increasing sample size, *J NeuroIntev Surg* **8**(1):104–110, 2016.
6. Sarrami-Foroushani A, Villa-Uriol M-C, Esfahany M, Coley S, di Marco L, Frangi A, Marzo A, Modeling of the acute effects of primary hypertension and hypotension on the hemodynamics of intracranial aneurysms, *Ann Biomed Eng* **43**:207–221, 2015.
7. Monson K, Goldsmith W, Barbaro N, Manley G, Axial mechanical properties of fresh human cerebral blood vessels, *J Biomech Eng* **125**:288–294, 2003.
8. Robertson A *et al.*, Diversity in the strength and structure of unruptured cerebral aneurysms, *Ann Biomed Eng* **43**:1502–1515, 2015.
9. MacDonald D, Finlay H, Canham P, Directional wall strength in saccular brain aneurysms from polarized light microscopy, *Ann Biomed Eng* **28**:533–542, 2000.
10. David D, Rica Nabong J, Rupture model of intracranial saccular aneurysms due to hypertension, *J Mech Med Biol* **15**:1550022, 2015.
11. Valencia A, Torres P, Rivera R, Galvez M, Bravo E, A mechanical study of patient-specific cerebral aneurysm models: The correlation between stress and displacement with geometrical indices, *Mech Res Commun* **36**:642–651, 2009.
12. Chung B, Cebral J, CFD for evaluation and treatment planning of aneurysms: review of proposed clinical uses and their challenges, *Ann Biomed Eng* **43**:122–138, 2014.
13. Torii R, Oshima M, Kobayashi T *et al.*, Fluid-structure interaction modeling of aneurismal conditions with high and normal blood pressures, *Comput Mech* **38**:482–490, 2006.
14. Chen J, Wang Sh, Ding G *et al.*, The effect of aneurismal-wall mechanical properties on patient-specific hemodynamic simulations: Two clinical case reports, *Acta Mech Sin* **25**:677–688, 2009.
15. Bazilevs Y, Hsu MC, Zhang Y *et al.*, Computational vascular fluid-structure interaction: Methodology and application to cerebral aneurysms, *Biomech Model Mechanobiol* **9**:481–498, 2010.

16. Takizawa K, Brummer T, Tezduyar TE, Chen P, A comparative study based on patient-specific fluid–structure interaction modeling of cerebral aneurysms, *J Appl Mech* **79**:010908-1–010908-13, 2012.
17. Sanchez M, Ambard D, Costalat V *et al.*, Biomechanical assessment of the individual risk of rupture of cerebral aneurysms: A proof of concept, *Ann Biomed Eng* **41**:28–40, 2012.
18. Costalat V *et al.*, Biomechanical wall properties of human intracranial aneurysms resected following surgical clipping (IRRAs Project), *J Biomech* **44**:2785–2691, 2011.
19. Valencia A, Burdiles P, Ignat M *et al.*, Fluid structural analysis of human cerebral aneurysm using their own wall mechanical properties, *Comput Math Methods Med* **2013**: Article ID 293128, 2013.
20. Pereira VM, Brina O, Gonzales A *et al.*, Evaluation of the influence of inlet boundary conditions on computational fluid dynamics for intracranial aneurysms: A virtual experiment, *J Biomech* **4**:1531–1539, 2013.
21. Xiang J, Siddiqui AH, Meng H, The effect of inlet waveforms on computational hemodynamics of patient-specific intracranial aneurysms, *J Biomech* **16**:3882–3890, 2014.
22. Valencia A, Contente A, Ignat M *et al.*, Mechanical test of human cerebral aneurysm specimens obtained from surgical clipping, *J Mech Med Biol* **15**(5):1550075, 2015.
23. Johnston B, Johnston P, Corney S, Kilpatrick D, Non-Newtonian blood flow in human right coronary arteries: Steady state simulations, *J Biomech* **37**:709–720, 2004.
24. Zamir M, *The Physics of Pulsatile Flow*, Springer, New York, 2000.
25. Olufsen M, Nadim A, On deriving lumped models for blood flow and pressure in the systemic arteries. *Math Biosci Eng* **1**:61–80, 2004.
26. Waite L, Fine J, *Applied Biofluid Mechanics*, McGraw-Hill, 2007.
27. ADINA, Theory and Modeling Guide, Vol. 1, Watertown, MA, USA, 2011.
28. Humphrey JD, *Cardiovascular Solid Mechanics, Cells, Tissues and Organs*, Springer, New York, 2002.
29. Cebral JR, Duan X, Chung BJ, Putman C, Aziz K, Robertson AM, Wall mechanical properties and hemodynamics of unruptured intracranial aneurysms. *Am J Neuroradiol* **36**:1695–1703, 2015.
30. Lee C, Zhang Y, Takao H, Murayama Y, Qian Y, A fluid–structure interaction study using patient-specific ruptured and unruptured aneurysm: The effect of aneurysm morphology, hypertension and elasticity, *J Biomech* **46**:2402–2410, 2013.
31. Cornejo S, Guzmán A, Valencia A, Rodriguez J, Finol E, Flow-induced wall mechanics of patient-specific aneurysmal cerebral arteries: Nonlinear isotropic versus anisotropic wall stress, *Proc Inst. Mech Eng, H J Eng Med* **228**:37–48, 2014.
32. Goh KL *et al.*, Ageing changes in the tensile properties of tendons: influence of collagen fibril volume fraction. *J Biomech Eng* **130**:0211011-1–0211011-8, 2008.
33. Goh KL *et al.*, Bimodal collagen fibril diameter distributions direct age-related variations in tendon resilience and resistance to rupture, *J Appl Physiol* **113**:878–888, 2012.
34. Goh KL, Listrat A, Béchet D, Hierarchical mechanics of connective tissues: Integrating insights from nano to macroscopic studies, *J Biomed Nanotechnol* **10**:2464–2507, 2014.
35. Wang H *et al.*, Apoptosis in capillary endothelial cells in ageing skeletal muscle, *Aging Cell* **13**:254–262, 2014.